Earth and Planetary Science Letters 623 (2023) 118410

Contents lists available at ScienceDirect

Earth and Planetary Science Letters

journal homepage: www.elsevier.com/locate/epsl

Sintering of vesiculating pyroclasts

J. Weaver [a], A. Lamur [b], T.D. Lea [a], F.B. Wadsworth [c], J.E. Kendrick [b], J. Schauroth [a], Y. Lavallée [b,*]

[a] Department of Earth, Ocean and Ecological Sciences, University of Liverpool, L69 3GP, UK
[b] Earth and Environmental Sciences, Ludwig-Maximilians-Universität München, Munich, Germany
[c] Earth Sciences, Durham University, Science Labs, DH1 3LE, UK

ARTICLE INFO

Article history:
Received 15 March 2023
Received in revised form 14 September 2023
Accepted 15 September 2023
Available online 20 October 2023
Editor: C.M. Petrone

Keywords:
porosity
permeability
fragmental
degassing
open-system
diffusion

ABSTRACT

Hot volcanic pyroclasts can sinter, vesiculate, and outgas in concert – a combination of processes which remains poorly constrained. And yet this combination of processes can occur coincidently during deposition from pyroclastic density currents, in conduit-filling pyroclastic debris, and in tuffisites. In many of these settings, it is the sintering-driven evolution of permeability that is key to gas transport through the evolving deposit. Here, we experimentally and theoretically investigate the evolution of the permeable networks during sintering of hot fragmental volcanic systems, which are hydrous and oversaturated at the experimental conditions. Firstly, we find that vesiculation results in shutting of the inter-granular porous network as bubble growth drives expansion of the particles into one another, destroying interconnected pores. Secondly, we observe that degassing by diffusion out of the particle edge results in contraction of the vesicular particles, re-opening pore spaces between them. Therefore, we find that vesiculation, and diffusive outgassing compete to determine both the intra-fragment vesicularity and the permeability during sintering. The development of intra-fragment vesicularity directly impacts the inter-fragment pore space and its connectivity, which decreases during vesiculation and subsequently increases during diffusive outgassing, prompting complex, non-linear permeability evolution.

The relative dominance of these processes is fragment size dependent; proportionally, fine fragments lose gas at a higher rate than coarser fragments during diffusive outgassing due to larger surface area to volume ratios. As the systems progress, larger fragments retain a higher proportion of gas and so attain greater vesicularities than finer ones – and therefore, the coarse fragmental pyroclasts experience a greater, yet transient, reduction in connected porosity and permeability. We suggest that where vesiculation is sufficient, it can lead to the complete loss of connected porosity and the sealing of permeable pathways much earlier than in a sintering-only system. Our results suggest that classical sintering models must be modified to account for these vesiculation and diffusive degassing processes, and that only a combined vesiculation, sintering, and diffusive outgassing model can resolve the evolution of permeability in hot clastic volcanic systems.

1. Introduction

Pyroclasts are a principal product of explosive volcanism. Upon eruption, pyroclasts are variably supersaturated in volatiles, and can therefore continue to degas as long as they remain sufficiently hot (e.g., Giachetti and Gonnermann, 2013). Similarly, if deposited hot, they can sinter and weld to form ignimbrites on the Earth's surface, or tuffisites and vent-filling welded breccias in volcanic conduits (Branney et al., 2002; Kolzenburg and Russell, 2014; Tuffen and Dingwell, 2005). It is the latter – vent-filling deposits and tuffisites – where sintering of hot pyroclasts can essentially clog the volcanic system and inhibit outgassing pathways (Kolzenburg and Russell, 2014; Wadsworth et al., 2020a), with implications for gas pressure build-up and subsequent explosive eruption triggering. Constraining the porosity and permeability evolution of these in-conduit welding systems is key for understanding volcanic activity and eruption cycles.

Hot pyroclasts – or melt fragments – may deposit (Saubin et al., 2016; Unwin et al., 2021), agglutinate due to sintering (Quane and Russell, 2005; Vasseur et al., 2013) or interface healing (Lamur et al., 2019), chemically evolve due to degassing-driven dehydration or resorption-driven rehydration (McIntosh et al., 2014; von Aulock et al., 2017), and physically deform due to shear, vesiculation, and densification (Ryan et al., 2015a; von Aulock et al., 2017).

* Corresponding author.
E-mail address: yan.lavallee@lmu.de (Y. Lavallée).

https://doi.org/10.1016/j.epsl.2023.118410

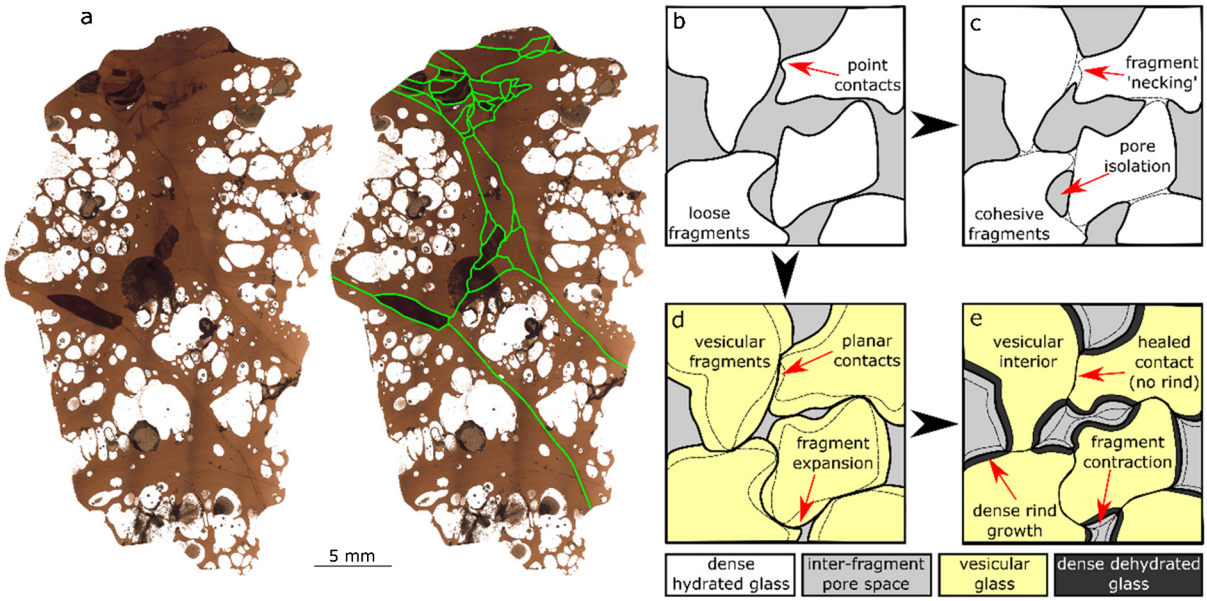

Fig. 1. Volumetric changes associated with vesiculation, diffusive outgassing, and sintering, shown in (*a*) photomicrograph of naturally sintered glass fragments from Hrafntinnuhryggur, Krafla volcano (Iceland), showing dense rinds, vesicular interiors (white), and fragment interfaces (highlighted in green on the right); (*b*) a sketch of an initially cohesionless fragmental melt; (*c*) sintered, fragmental melt which is anhydrous; (*d*) hydrous fragmental melt which develops vesicularity at the expense of the interstitial pore space, followed by (*e*) diffusive outgassing which creates a dense, bubble-free rind which progressively densifies the vesicular melt fragments.

It is clear that all of these processes are relevant in natural volcanic settings, and yet, they are typically investigated in isolation, such that the competition between each process is not well understood. Here, we investigate how the interactions between sintering, vesiculation, and diffusive outgassing of hot pyroclasts impact the evolution of porous, permeable networks and consider the implications for fragmental volcanic systems.

Sintering describes the densification of a loose particulate aggregate into a cohesive, variably porous material through diffusional and viscous processes (e.g., Wadsworth et al., 2019). The evolution and timescales of sintering silicate melt fragments [synthetic, e.g., Wadsworth et al. (2016a); or fine volcanic glass particles, e.g., Gardner et al. (2018) and Wadsworth et al. (2019)] can be modelled using validated theory (Wadsworth et al., 2016a). This theory shows that at low pressures, sintering is controlled by the viscosity of the melt, the size of the pore spaces between the grains (which is related to the grain size), and the melt-gas interfacial tension (Wadsworth et al., 2019, 2016a). The resultant permeability of sintering and densifying networks is determined by the connectivity and surface area of the inter-fragment pore space (e.g., Wadsworth et al., 2016b); direct observation and modelling indicate that permeability reduction is non-linear, as the fragmental system undergoes topological inversion (Wadsworth et al., 2017b). However, the previous work in which this theory is tested has focussed on systems in which the melt fragments are not vesiculating during sintering.

Vesiculation occurs in melt fragments when they are supersaturated in volatiles, leading to bubble nucleation and growth (Coumans et al., 2020; Giachetti et al., 2010; Navon and Lyakhovsky, 1998; Sparks, 1978). Quenched volcanic products demonstrate that vesiculation occurs in sintered pyroclasts (Fig. 1a). Under closed-system conditions, the porosity of a vesiculating melt fragment is captured by bubble growth models (Bagdassarov et al., 1996; Coumans et al., 2020), which show that bubble growth leads to a bulk volume increase until equilibrium (e.g., Blower et al., 2001). In molten particulate systems, we anticipate that vesiculation and the volumetric expansion of pyroclasts would occur at the expense of the connected pore volume between fragments (Fig. 1b-e).

Diffusive outgassing refers to gas loss from melt fragments. In open-system conditions, volatile equilibrium in the melt may be modified by the entrainment, mixing, or fluxing of atmospheric and volcanic gases (Ohsawa et al., 2000; Rust et al., 2004). This can create partial pressure differences between the melt and the connected pore space, prompting chemical exchange (von Aulock et al., 2017). Experiments have shown that diffusive volatile loss through the surface of vesiculating melt fragments causes marginal volatile resorption and bubble shrinkage, promoting the development of a dense, dehydrated rind, which thickens at a rate predicted by the diffusion length (Otsuki et al., 2015; von Aulock et al., 2017; Weaver et al., 2022; Yoshimura and Nakamura, 2008). This is analogous to resorption processes, which reduce vesicularity and cause fragments to densify (Weaver et al., 2022). The effective rate of diffusive outgassing is sensitive to the surface area of melt fragments (Otsuki et al., 2015), such that the size of fragments controls the efficacy of diffusive outgassing and the vesicularity evolution.

When occurring together, vesiculation and diffusive outgassing may compete to expand and contract melt fragments, at different rates, depending on the sizes of fragments present in the aggregate material (Weaver et al., 2022). Textural analysis commonly captures this competition in sintering fragmental environments, where dense rinds surround parcels of vesiculated melt (cf. Cabrera et al., 2011; Castro et al., 2012; Giachetti et al., 2021; Heap et al., 2019; Saubin et al., 2016; Fig. 1). To a first order approximation, this competition can be assessed through a fragment size dependent Peclét number Pe, which is determined by the ratio of the timescales required for diffusive outgassing and vesiculation to complete (see Weaver et al., 2022 for further details). Where $Pe \ll 1$, vesiculation may be inhibited by the complete diffusive outgassing of supersaturated volatiles and sintering may proceed following anhydrous melt dynamics; whereas, if $Pe \gtrsim 1$, vesicles form and are subsequently resorbed until all bubbles are lost or the densification is otherwise interrupted (e.g., by cooling). Therefore, sintering fragmental systems with $Pe > 1$ will be variably impacted by vesiculation and diffusive outgassing, which may play a decisive role in the evolution of permeable porous networks, and possibly influence the transition between open and closed gas-venting systems. Here, we experimentally investigate and mon-

itor the porosity and permeability development during sintering of vesiculating and outgassing melt fragments of various sizes (i.e., various Pe), and assess the power of an integrated sintering, vesiculation, and diffusion model in capturing this complex evolution.

2. Material and methods

2.1. Material and experiment setup

For our experiments, we selected a well-studied aphyric, vesicle free, calc-alkaline rhyolitic glass from Hrafntinnuhryggur, Iceland (Ryan et al., 2015a, 2015b; Tuffen and Castro, 2009; Wadsworth et al., 2021, 2019). We used the same sample material as in Weaver et al. (2022) and Seropian et al. (2022), wherein, the geochemical composition of the glass was determined by X-ray fluorescence and the water content was measured using FTIR at 0.10±0.02 wt.%. The block was manually crushed into irregular-shaped fragments which were sieved to four size ranges to provide a range of Pe conditions (see Section 4.1). The fragment size ranges, 0.50–1.00 mm, 1.00–1.40 mm, 1.40–2.00 mm and 2.00–2.36 mm, are henceforth referred to by their average diameters of 0.75 mm, 1.20 mm, 1.70 mm, and 2.18 mm, respectively. The crushed glass was cleaned in an ultrasonic water bath and oven dried at 50 °C to remove any adsorbed water. Crucibles were fashioned out of dense holocrystalline basalt from Seljavellir, Iceland (rock described in Lamur et al., 2018) by coring 50 mm-long hollow cylinders with internal and external diameters of 18.6 mm and 26 mm, respectively. The base of each tube was closed using a detachable disk-shape, base plate of the same basalt. Prior to testing, the crucible assemblies were thermally treated at 1006 °C for 6 hours to ensure no physico-chemical alteration would occur during the experiments. For the experimental samples a 13 g aliquot of loose fragments of a single size range were placed into a crucible, which was gently shaken to encourage a uniform packing density. Each glass-filled crucible was heated individually to 1006 °C at 10 °C.min^{-1} in a Carbolite® box furnace. The assemblies were left to dwell at this isotherm for 0.5 to 24 hours, before being cooled to room temperature at 10 °C.min^{-1}. The resultant products were then subjected to porosity and permeability measurements, and select samples were embedded in epoxy, sliced, and imaged using a Hitachi TM3000 scanning electron microscope operating at 15 kV.

2.2. Volume and porosity determination

The pore space evolution is complex in these experiments. Isolated porosity is fully enclosed within the melt (i.e., as vesicles), between extensively sintered fragments, or trapped by melt fragments agglutinated against the crucible, and cannot contribute to permeable flow through the assembly. Conversely, connected porosity retains system-wide permeable pathways. The inter-fragment porosity can be either isolated or connected, depending on the degree of sintering and pore closure. To quantify the development of porosity the volumetric evolution of the samples and pore space was measured for each experimental product (conducted with different fragment sizes over various dwell times) using an AccuPyc 1340 helium pycnometer from Micromeritics, accurate to ±0.1% of the measured volume. Prior to an experiment the skeletal volume of each crucible V_B was measured. After being filled with crushed glass, the skeletal volume of each pre-experimental sample assembly V_{BGo} was measured, and, following an experiment, the skeletal volume of each sample and crucible V_{BGp} was measured again. The skeletal volume of the experimental glass products V_{Gp} is then given by $V_{Gp} = V_{BGp} - V_B$. Then, the isolated porosity of the sample ϕ_i was calculated using Equation (1):

$$\phi_i = 1 - \frac{V_{BGo} - V_B}{V_{Gp}}. \quad (1)$$

This method assumes that the pre-experimental glass fragments did not contain vesicles (see Supplementary Figure 1).

The original height of the glass fragment aggregate was measured, which along with the crucible inner diameter, was used to constrain the initial bulk cylindrical volume of the crushed glass and pores V_{To}. The post-experimental height of the sintered aggregate was also measured, which was used to obtain the bulk cylindrical volume of the sintered sample V_{Tp}. These allowed us to calculate the connected porosity of the glass particulate before ϕ_{co} and after ϕ_{cp} the experiments, via:

$$\phi_{c(n)} = 1 - \frac{(V_{BG(n)} - V_B)}{(V_{T(n)})}, \quad (2)$$

where the subscripts (n) maybe be replaced with o or p for pre- (original) or post-experiment samples, respectively.

Finally, the total porosities of the pre- and post-experiment sample aggregates (i.e., the combined isolated and connected pore space), ϕ_{to} and ϕ_{tp}, respectively, were determined for each sample using:

$$\phi_{t(n)} = 1 - \frac{V_{BGo} - V_B}{V_{T(n)}}. \quad (3)$$

2.3. Permeability measurements

To evaluate the permeability of the experimental products, steady state measurements were conducted using a synthetic oil with a density of 862.4 kg.m^{-3}. For these measurements, the base of the sample assembly was removed (leaving the basalt tube and sintered fragments), and the assembly was saturated in oil for 24-hours using a vacuum chamber at 0.1 bar. Following Wadsworth et al. (2020b), the saturated assembly was placed upright into a tight-fitting Viton® sleeve with a 25 mm inner diameter and extending 26 cm above the sample. The sleeve was then filled with oil, which applied 2.2 kPa of hydraulic head pressure to the sample. As oil percolated through the sample, the pressure was manually maintained for 10 minutes by continuously refilling the top of the sleeve. The relatively slow percolation of oil through the sample allowed the oil level to be maintained to within ~2 mm of the target head height. We measured the amount of oil passing through the sample using a digital balance and determined the flow rate, from which we calculated permeability using Darcy's law, considering an oil viscosity of 381 mPa.s. We consider that oil was only able to pass through the sintered material, so the effective surface area for fluid flow was limited to the inner diameter of the basalt tube. To verify this, and to check for leakage between the tube and the outer surface of the basalt tube, we prepared a specimen of the same Seljavellir basalt [with a known gas permeability of 5×10^{-20} m^2 (Lamur et al., 2018)], with the same dimensions as used for the sample crucibles, but with no central bore. We placed this solid core into the same permeability assembly, and found that no oil was able to pass through the sample over a 24-hours observational period.

Uniquely, the sample with 1.20 mm grain size and a dwell time of 21,600 s was able to be detached from the basalt crucible, and thus, additional measurements were performed under confining pressure using a benchtop Gasperm permeameter from Vinci Technologies with nitrogen gas. The sample was inserted into a rubber sleeve and placed into the Gasperm. We applied a confining pressure of 1 MPa, and set 5 consecutive flow rates of 100–500 cm^3 min^{-1}, with 100 cm^3 min^{-1} intervals. We recorded the pressure differential from inlet to outlet at each flow interval, in order to use Darcy's law to calculate permeability. We then used the average permeability obtained at the 5 flow rates.

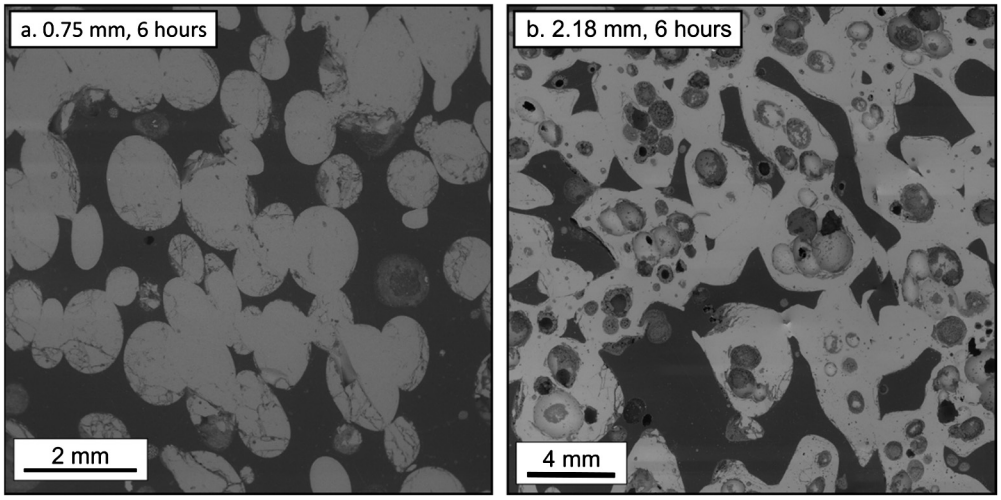

Fig. 2. Representative backscatter electron images of the experimental products. Melt fragments (pale grey) vesiculate and are subsequently densified by diffusive outgassing. Finer fragments with low Pe (a) lose vesicularity faster than coarse, high Pe fragments. (b) High vesicularity is associated with lower and less connected inter-fragment pore space (dark grey) – note the different scale of the images.

3. Results

In this study we conducted 59 experiments, the details of which are reported in Supplementary Table 1. Within the evolving particulate systems, we observe changes to the porous network, including the isolated, connected, and total porosities. The time-dependence of these properties depends on the fragment size. Through textural analysis, we find that each melt fragment grows bubbles and develops an encompassing dense rind which thickens with time. The melt fragments begin to agglutinate and fragment necks form, as sintering ensues, which reduces the connectivity of pore space. Phenomenologically, the volume and connectivity of the inter-fragment pore space also decreases with bubble growth and subsequently increases through fragment densification, the latter of which occurs faster in finer fragments relative to coarser fragments (Fig. 2).

These processes are captured quantitatively through volume and permeability measurements from the time-series products. The pre-experimental melt is vesicle free and so initially there is no isolated pore space. Upon dwelling at the experimental temperature, the sample isolated porosity rapidly increases to a peak as the particles vesiculate, before it more slowly decreases and returns to zero (Fig. 3a). The peaks and durations of the porosity curves positively correlate with the fragment size; the 0.75 mm samples increase in the first 3,600 s to a peak of ∼5 vol.%, and then return to, and remain at ∼0 vol.% after 21,600 s of heating; the 1.20, 1.70, and 2.18 mm samples increase for the first 7,200 s to maximum values of ∼10, 25, and 33 vol.%, respectively. Subsequently, the isolated porosities decrease, with the 1.20 mm samples returning to near zero values after 43,200 s of heating, whilst the 1.70 mm and 2.18 mm samples required heating times between 43,200 s and 86,400 s to approach 0 vol.%.

The initial connected porosities average 49 ± 2.8 vol.% across all samples and show no fragment size control. However, the evolution of connected porosity is dependent on fragment size and mirrors the isolated porosity evolution; the connected porosities decrease to a minimum, before increasing and returning to values approaching their pre-experimental porosities (Fig. 3b). The connected porosities of the 0.75 mm, 1.20 mm, 1.70 mm, and 2.18 mm samples decrease for the first 7,200 s to ∼42, 40, 28, and 20 vol.%, respectively. Following this, the connected porosities increase until 21,600 s for the 0.75 mm samples, 43,200 s for the 1.20 mm and 1.70 mm samples, and 86,400 s for the 2.18 mm samples. For the three finer populations, the connected porosities then slightly decrease until the end of observation. Due to the initial absence of vesicles, the total porosities are initially equal to the connected porosities. The total porosities show that the fragmental systems generally densify over the timescale of our observations, yet the paths taken contrast markedly and show subtle fragment-size dependencies (Fig. 3c). The 0.75 mm and 1.20 mm samples experience relatively constant total porosities for 21,600 s before porosity loss accelerates; by contrast, the 1.70 mm and 2.18 mm samples experience a total porosity increase between 1,800 s and 7,200 s, followed by porosity loss for longer isothermal durations. After the longest dwell period of 86,400 s the final total porosity reduction appears dependent on fragment size, with the coarser fragments showing more significant densification (Fig. 3c).

The observed non-linear changes in connected porosity result in a complex temporal evolution in unconfined permeability, the values of which develop as a function of fragment size (Fig. 3d). The first measurements after 1,800 s reveal higher permeabilities for coarser fragment sizes. There is however, less than one log unit in variability across the entire sample suite. Subsequently, the permeabilities of the 0.75 mm samples increase briefly before stabilising. In contrast, the permeabilities of the 1.20 mm samples decrease for the first 3,600 s, before subsequently increasing over longer timescales to values comparable with the initial 1,800 s measurement. The coarser 1.70 mm and 2.18 mm samples experience a greater permeability reduction for the first 7,200 s, before also subsequently increasing. The extent of permeability reduction, and the time required to reach the lowest value, increase with fragment size. Permeability is approximately 1 order of magnitude lower for the sample measured under 1 MPa confining pressure in the gas permeameter (Fig. 3d & Supplementary Table 2).

We observe the porosity evolution of our samples is substantially different than would be anticipated for the densification of non-vesiculating systems during sintering (Fig. 3). We illustrate this deviation by comparing our sample porosity data to the sintering model of Wadsworth et al. (2016a), using the average sieve grain size for each population (0.75 mm, 1.20 mm, 1.70 mm, and 2.18 mm) to estimate the average pore size (65 μm, 104 μm, 148 μm, 190 μm for equivalent monodisperse, spherical particles; following Wadsworth et al., 2016a), a melt-vapour surface tension Γ equal to 0.3 $N.m^{-1}$ (Parikh, 1958), a melt viscosity μ equal to 3.47×10^7 Pa.s, as modelled using our initial sample water content and the experimental temperature (Hess and Dingwell, 1996), and a monodisperse pore size correction (Wadsworth et al., 2017a). Likewise, we illustrate the permeability deviation using the out-

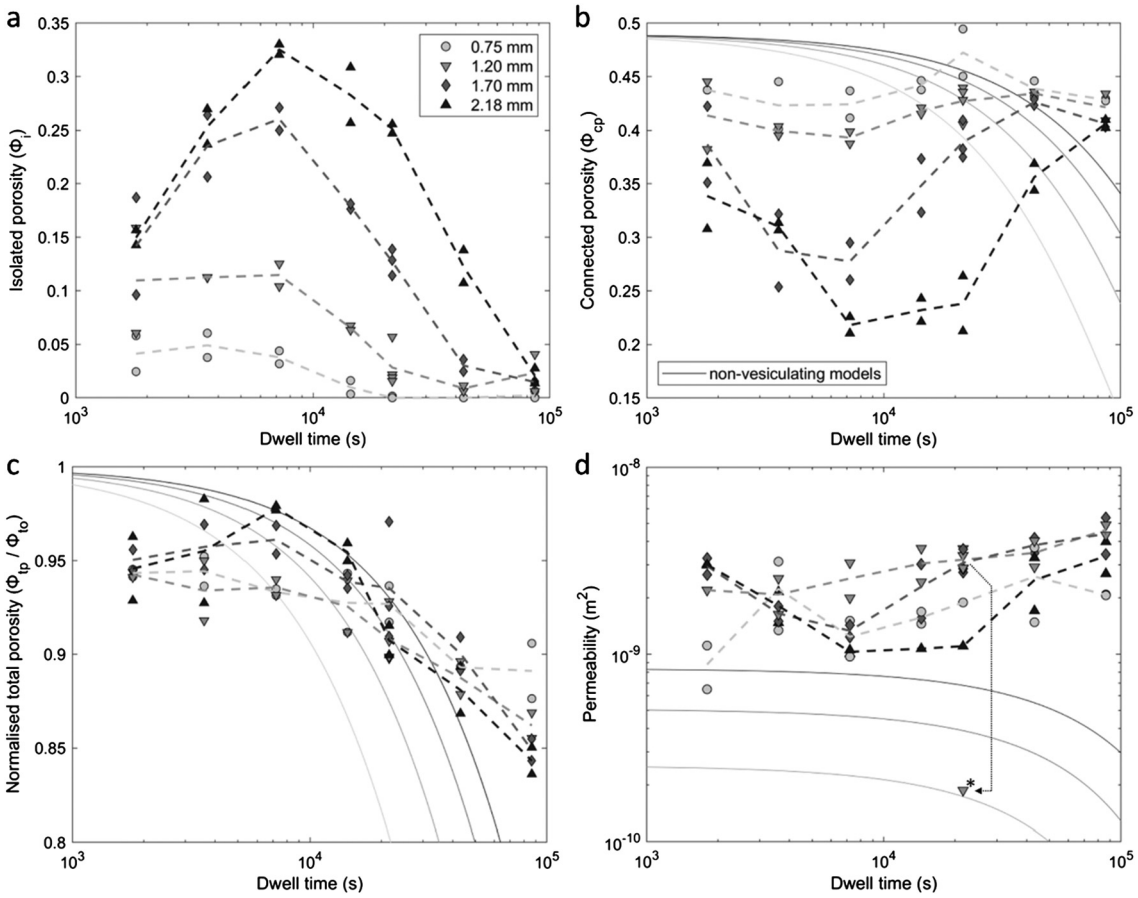

Fig. 3. Evolution of the porous permeable network during sintering of vesiculating and diffusively outgassing pyroclasts. The systems experience fragment-size dependent evolution in (*a*) isolated porosity ϕ_i, (*b*) connected porosity ϕ_c, (*c*) normalised total porosity, and (*d*) permeability. For each fragment size, a dashed line connects the average value for each time increment. The sample data are compared to non-vesiculating models (solid line colours correspond to the modelled fragment size) for densification during sintering (Wadsworth et al., 2016*a*), the results of which are used in the presented permeability models (Wadsworth et al., 2016*b*). The one sample permeability remeasured with a confining pressure of 1 MPa is highlighted with an asterisk (*) in panel d.

puts of the non-vesiculating porosity modelling, in conjunction with a universally scaled permeability model (Wadsworth et al., 2016b). Therein, we estimate the specific surface area S of our fragments using the average grain size for that population, and include a factor of 1.2 to account for the irregular fragment shape, as defined by Wadsworth et al. (2021). We note that this model was developed for permeability measurements conducted with confining pressure (Wadsworth et al., 2016b), thus, the absolute values of our unconfined measurements are expected to be offset to higher permeabilities. Our permeability measurement made with confining pressure is more directly comparable to the modelled permeability, though we are cautious to interpret absolute values due to our limited measurements under confinement. Due to the different conditions of the measurements, here, our interest lies in the differences in evolution between the experimental and modelled permeability trends through time rather than the absolute values. The marked differences between the trends of our data and these models which only account for sintering under non-vesiculating conditions, suggest that an approximate estimate for permeability evolution in hydrous fragmental systems demands an understanding of inter- and intra-granular porosity development during simultaneous sintering, vesiculation, diffusive outgassing.

4. Discussion

In the high-temperature experiments presented here, the pyroclasts are oversaturated in H_2O, which drives the growth of vesicles that is observed in some run products (e.g. Fig. 2b) coupled with a large isolated porosity development (Fig. 3). However, it is clear that the finest pyroclasts used here do not preserve vesicles in all run products (Fig. 2a) and do not record a marked increase in isolated porosity. Following Weaver et al. (2022), we associate this grain-size dependence with the diffusive loss of volatiles from the pyroclast surface, which occurs due to the lower partial pressure of H_2O in the laboratory atmosphere, relative to the melt and isolated vesicles (von Aulock et al., 2017). This lower partial pressure outside the pyroclasts compared with inside results in a chemical exchange such that H_2O will diffuse to the atmosphere adjacent to the pyroclasts, and then percolate out from between the pyroclast aggregate into the laboratory atmosphere. The surface area of pyroclasts controls the efficiency of this diffusive loss, such that finer pyroclasts will diffusively outgas proportionally more, and therefore faster, than coarser fragments. For very fine pyroclasts, diffusive outgassing may lower the water content of the melt below the solubility limit, before vesicles have the time to form and grow. However, in moderately sized pyroclasts diffusive loss to the outside occurs while vesicles form and grow beyond the diffusion front, resulting in rinds forming from the outside inward of otherwise expanding vesicular pyroclasts. If the process is not interrupted by cooling or equilibration of the gas partial pressures, eventually even large particles will become vesicle-free again by diffusive losses but will have vesiculated in the intervening time. In the experiments presented here (Fig. 3), these processes are occurring with the same complexity found by von Aulock et al. (2017) and Weaver et al. (2022). However, here, the particles are (1) in a many-particle system that can sinter together while vesic-

ulation and diffusive outgassing occur, and (2) in a confined geometry such that the wholesale expansion of vesiculating particles causes particle-particle flattening. This confers additional complexity relative to that studied by Weaver et al. (2022), with additional dynamics and associated timescales to consider. As such, here we first set out to evaluate the relative timescales of vesiculation, diffusive outgassing, and sintering, in order to constrain when they operate and dominate during the evolution of pyroclasts agglutinates in our experiments.

4.1. Timescales of vesiculation, diffusive outgassing, and sintering

The vesiculation timescale τ_b is the time required for bubble growth to fully degas the fraction of volatiles in excess of saturation (i.e., when a parcel of magma reaches its maximum vesicularity without diffusive outgassing). We estimate the vesicularity evolution for our samples using the bubble growth model by Coumans et al. (2020), and select τ_b where the vesicularity asymptote is reached. We run the bubble growth model using our initial sample water content (0.1 wt.% H_2O) and experimental temperature and pressure conditions, as well as a bubble number density of 4.63×10^{10} m^{-3}, following Weaver et al. (2022). Within the bubble growth model, we employed the models for the equation of state of gas, volatile solubility, diffusivity, and melt viscosity developed by Pitzer and Sterner (1994), Ryan et al. (2015b), Zhang and Ni (2010), and Hess and Dingwell (1996), respectively. In detail, the Coumans et al. (2020) model solves for the full bubble growth dynamics, and as such the bubble growth may be in a diffusive or viscously limited regime, but here this is simply captured by the output τ_b timescale.

The diffusive outgassing timescale τ_d gives the time required for volatile loss out of the pyroclast edges, which is equivalent to the dense rind consuming the full fragment. We approximate the rind thickness d_l over time t by using a diffusion lengthscale $d_l(t) = K\sqrt{Dt}$ (von Aulock et al., 2017). Here, K is a scaling factor, which for our sample size populations, was empirically constrained at 2.7 (Weaver et al., 2022). D is the diffusion coefficient of H_2O in the melt. We estimate D using the model provided by Zhang and Ni (2010), considering the pressure and temperature conditions in our experiments, and the initial H_2O concentration in the melt. Diffusive outgassing completes when d_l equals the minimum radius of the sample. However, the fragment sizes for each of our populations are determined by a sieve opening range (e.g., 0.5–1 mm), which poorly constrains the radii of our irregular fragments, and so we have uncertainty on τ_d. To account for this, we calculate apparent fragment radii, $r = 3S^{-1}$, which, as the specific surface area S is determined by an irregular fragment approximation (Wadsworth et al., 2021), would correlate to their equivalent spherical surface area to volume ratios. For our four fragment size populations, we calculate r ranges equal to 0.21–0.42, 0.42–0.58, 0.58–0.83, and 0.83–0.98 mm. We then calculate τ_d when the diffusion length scale equals r, such that $\tau_d = r^2/(K^2D)$, following Weaver et al. (2022). The Peclét number Pe, is determined by the ratio of the diffusive outgassing and vesiculation timescales, such that $Pe = \tau_d/\tau_b = r^2/(\tau_b DK^2)$. As discussed in Weaver et al. (2022), $Pe \ll 1$ implies that diffusion is rapid and that the particles will not form bubbles internally before the particle equilibrates H_2O by diffusion instead. And $Pe \gg 1$ implies that diffusion is sluggish compared with bubble growth such that bubbles will form inside the particles. However, $Pe \gg 1$ does not capture the fact that at very long times $t \rightarrow \tau_d$, diffusion will still occur and result in dense particles at low H_2O, albeit particles that have been through a cycle of vesiculation and densification (Weaver et al., 2022).

Finally, the sintering timescale for shallow, surface tension-dominated melt fragments is given by $\tau_s = a_o\mu C/\Gamma$ (Wadsworth et al., 2019), where a_o is the initial radius of the pores between the packed particles [computed using the model provided in Wadsworth et al. (2016b)], C is a correction factor, accounting for the fact that we use a monodisperse particle size in a model that is most accurate for continuous polydisperse systems (computed using Wadsworth et al., 2017a), and μ is the viscosity. Here, as we consider a degassing system, and given that viscosity depends on the local H_2O in the melt, we anticipate that the viscosity will be transient (Hess and Dingwell, 1996) which will impact the sintering timescale. As such, we consider that the sintering timescale may vary between that predicted for the initially hydrated sample ($\tau_{s(wet)}$), and for the late, dehydrated sample ($\tau_{s(dry)}$), which, following von Aulock et al. (2017), experience 20% partial pressure of water in the furnace compared to the atmosphere; this provides an open system equilibrium for the H_2O concentration in the melt equal to 0.039 wt.%. Wadsworth et al. (2019) provide a solution for sintering that does account for this diffusive loss of H_2O out of the particles, whereas here we simply bracket our estimated timescales by the two end-members $\tau_{s(dry)}$ and $\tau_{s(wet)}$, respectively.

Comparing the timescales for the completion of sintering, vesiculation, and diffusive outgassing (Table 1; Fig. 4a) constrains which processes complete and/or dominate in our experiments. We note that sintering and diffusive outgassing are size dependent processes and occur from the start of the experiment until their completion time; conversely, vesiculation is not fragment size dependent, but has a time-lag, delaying its onset (we term the onset $\tau_{b(0)}$). Therefore, the relative position of these timescales establishes different scenarios relevant for our experimental conditions, as defined by pyroclast size:

Regime I: $\tau_d < \tau_{b(0)}$ (i.e., $Pe \ll 1$) and $\tau_d \ll \tau_s$ – very fine pyroclasts fully outgas before bubbles nucleate, followed by the sintering of the dehydrated melt;

Regime II: intermediate sized fragments, where $\tau_d < \tau_b$ (i.e. $Pe < 1$) and $\tau_d < \tau_s$, – vesiculation and diffusive outgassing compete concurrently to expand and densify the melt fragments, respectively. Because $\tau_d < \tau_b$, the fragments fully outgas before vesiculation completes. Once τ_d is reached all vesicularity is lost and the dehydrated melt continues to sinter;

Regime III: intermediate sized fragments, $\tau_d > \tau_b$ (i.e., $Pe > 1$) and $\tau_d < \tau_s$, – similar to regime II, vesiculation and diffusive outgassing occur concurrently, however here, vesiculation reaches its closed system equilibrium prior to losing all vesicularity through diffusive outgassing. Again, sintering of the dry melt completes last;

Regime IV: coarse fragments, where $\tau_d \gg \tau_b$ (i.e., $Pe \gg 1$) and $\tau_d > \tau_s$, – vesiculation reaches equilibrium with little impact from diffusive outgassing. Sintering also dominates over diffusive outgassing and the associated rind growth, leading to sintered melt aggregates which are variably vesiculated and hydrous.

We suggest that for all four regimes, a dense rind will form which, even when thin relative to the fragment radius, will influence the inter-fragment dynamics and so, these openly outgassing sintering pyroclasts should be assessed using $\tau_{s(dry)}$, which increases the fragment size range over which regimes II and III are applicable (Fig. 4b). We note that τ_d is largely unaffected by dehydration for our samples which originally contained only 0.1% water (Table 1), but, for more hydrous samples, τ_d may vary significantly (Weaver et al., 2022). We stress that, with the exception of τ_b which is computed explicitly from a full model, the timescales outlined in Fig. 4a provide the approximate, characteristic time required for the completion of each process. Vesiculation, diffusive outgassing, and sintering progress non-linearly, and remain

Table 1
The timescales for the completion of vesiculation τ_b (closed system), diffusive outgassing τ_d, and sintering τ_s for each of our sieved fragment size R, and for the initial, and the two end-state degassed conditions. The results are particularly dependent on the melt water content, the diffusion coefficient D, and the melt viscosity μ. The Peclét number Pe normalises the diffusive outgassing timescale to vesiculation timescale to assess the dominant mode of volatile redistribution.

R (mm)	τ_b (s)	τ_d (s)	τ_s (s)	$Pe = \tau_d/\tau_b$
Initial sample conditions, - 0.1 wt.% H_2O, $D = 7.01 \times 10^{-13}$, $\mu = 3.47 \times 10^7$ (wet)				
0.50	9×10^3	8.48×10^3	1.05×10^5	0.94
1.00	9×10^3	3.39×10^4	2.10×10^5	3.77
1.40	9×10^3	6.65×10^4	2.94×10^5	7.39
2.00	9×10^3	1.36×10^5	4.13×10^5	15.08
2.36	9×10^3	1.89×10^5	4.96×10^5	21.00
Closed-system equilibrium, - 0.088 wt.% H_2O, $D = 6.18 \times 10^{-13}$, $\mu = 4.44 \times 10^7$ (intermediate)				
0.50	9×10^3	9.64×10^3	1.35×10^5	1.07
1.00	9×10^3	3.86×10^4	2.70×10^5	4.28
1.40	9×10^3	7.56×10^4	3.78×10^5	8.40
2.00	9×10^3	1.54×10^5	5.30×10^5	17.14
2.36	9×10^3	2.15×10^5	6.36×10^5	23.86
Open-system equilibrium, - 0.039 wt.% H_2O, $D = 6.18 \times 10^{-13}$, $\mu = 1.99 \times 10^8$ (dry)				
0.50	9×10^3	9.64×10^3	6.05×10^5	1.07
1.00	9×10^3	3.86×10^4	1.21×10^6	4.28
1.40	9×10^3	7.56×10^4	1.69×10^6	8.40
2.00	9×10^3	1.54×10^5	2.38×10^6	17.14
2.36	9×10^3	2.15×10^5	2.86×10^6	23.86

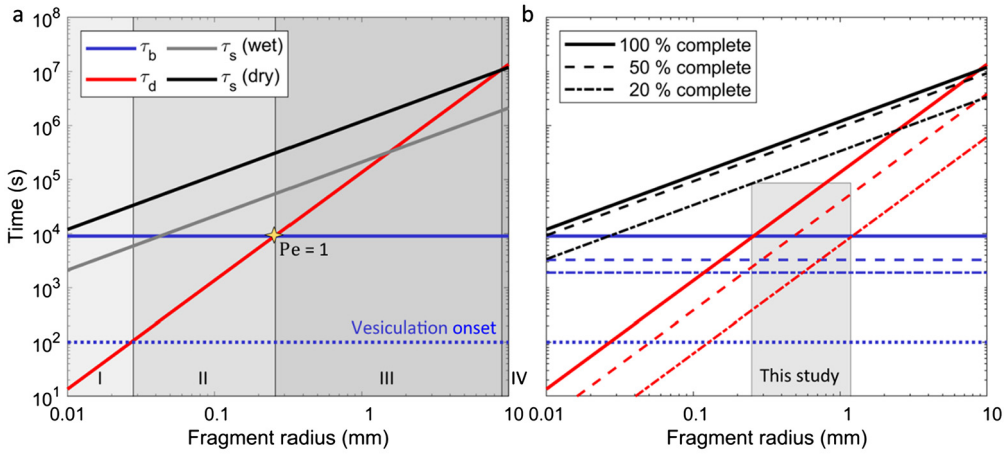

Fig. 4. Timescales of vesiculation τ_b, diffusive outgassing τ_d, and sintering τ_s (wet and dry). (*a*) melt fragments may reach the time required for each process to complete in different orders, depending on the fragment size of the aggregates. In regime I, fragments diffusively outgas before the onset of vesiculation (blue dotted line), followed by sintering of dehydrated fragments $\tau_{s(dry)}$ (*i.e.* $\tau_{s(wet)}$ is no longer relevant in this regime); in regime II, vesiculation and diffusive outgassing occur concurrently, but the fragment fully outgasses before vesiculation and sintering complete (Pe < 1), and sintering is the final processes to complete; similarly, in regime III, vesiculation and diffusive outgassing occur concurrently, but here, vesiculation completes before diffusive outgassing (Pe > 1), and sintering is the final processes to complete; in regime IV, fragments vesiculate to their fullest extent and the inter-particle pore spaces seal through sintering before completion of diffusive outgassing. (*b*) Progression of vesiculation (blue lines), diffusive outgassing (red lines), and sintering (black lines). These processes progress to completion in a non-linear fashion; the progress of vesiculation is based on vesicularity (*e.g.*, 20% complete is equivalent to 20% of the final, closed-system vesicularity), the progress for diffusive outgassing is based on the closed-system water content evolution and is predicted by the model for rind growth (*e.g.*, 20% denotes where the rind thickness equals 20% of the fragment radius), and the progress of sintering is taken from the modelled results for our samples, using Wadsworth et al. (2019), when the initial connected porosity is reduced by one fifth (*i.e.*, 20%) and by half (*i.e.*, 50%).

active from their onset until reaching their respective completion timescale (Fig. 4b). In the next sections, we invoke these regimes to resolve the processes responsible for the observations made in our experiments.

4.2. Porosity and permeability hysteresis

Our experiments are contained by the intermediate regimes II and III defined above (see the grey box in Fig. 4a), whereby we expect vesiculation and fragment size dependent diffusive outgassing to compete before the system densifies substantially through sintering. In our samples, bubble growth during vesiculation rapidly creates isolated porosity, which increases the skeletal volume of the fragments at the expense of inter-fragment pore space (Fig. 5); conversely, marginal bubble resorption during diffusive outgassing slowly densifies the skeletal volume and increases the inter-fragment pore space. We find that this competition is controlled by fragment size, where a systematic shift in the vesicularity evolution of our samples creates non-unique, fragment size dependent hysteresis in porosity and permeability (Fig. 5).

Diffusive outgassing is less effective for systems of coarser fragments compared with systems of finer fragments. This means that for relatively coarser fragment sizes, vesiculation is increasingly dominant, which results in greater isolated and connected porosity changes before experiencing densification due to diffusive outgassing (compare Fig. 5a with 5d). The more substantial reduction in connected porosity due to vesiculation develops increasingly clear permeability relationships in coarser fragmental melts (compare Fig. 5e with 5h). However, diffusive outgassing continues to occur after vesiculation has completed, causing continual fragment densification due to volatile resorption until the time τ_d is reached

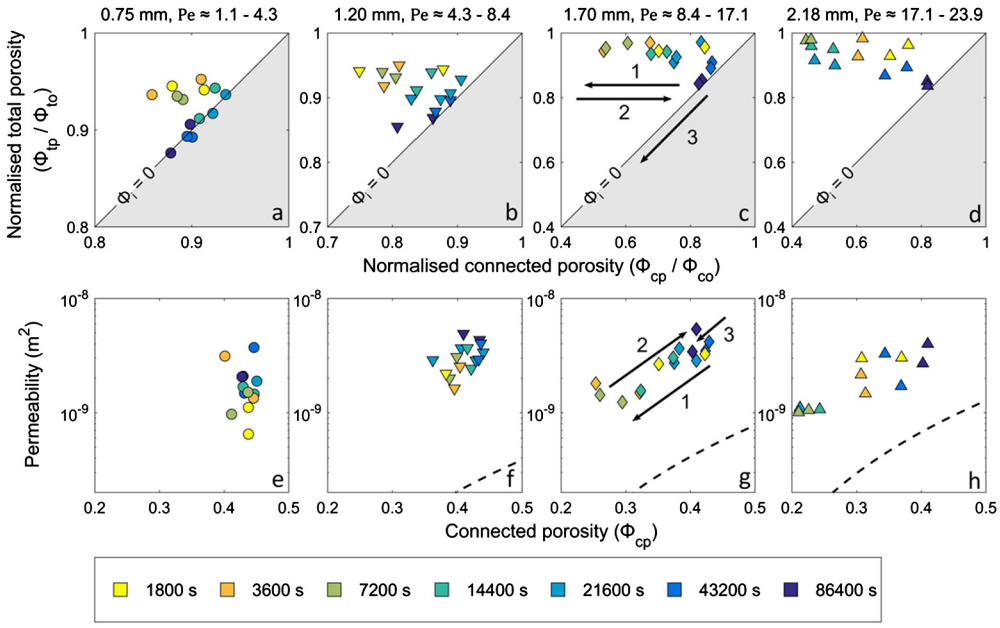

Fig. 5. Porosity and permeability hysteresis is dependent on fragment size (average diameter 0.75; 1.20; 1.70 and 2.18 mm, in panels a-d and e-h respectively). Here, ϕ_c and ϕ_t are the connected and total porosities, where o denotes the value prior to heating and p is the value following heating. In steps (as shown by the numbered arrows); (1) coarser fragments develop more vesicularity [porosity is isolated, as the data move away from the $\phi_i = 0$ line (panels a-d)], at the expense of connected porosity and permeability (panels e-h). (2) diffusive outgassing densifies melt fragments until the isolated porosity is lost, which increases the connected porosity and permeability; and (3) sintering densifies the full system, reducing the total and connected porosities, which are approximately equal. The densification through sintering is minor at these timescales, and so permeability shows little effect. The permeability model of Wadsworth et al. (2016b) is presented as a dashed line. Note the differing scales on normalised total and connected porosities; the same data is plotted with all axes set to equal scales in Supplementary Figure 2.

(see Fig. 2a); this enhances connected porosity and permeability (e.g., Fig. 5h).

The behaviour described here is complicated by the observation that sintering acts to progressively densify the system (e.g., Fig. 3c) and close the connected porosity, thereby reducing permeability and increasing τ_d. At short timescales relative to the sintering timescale (where vesiculation and diffusive outgassing operate), the resultant expansion and then densification of hydrous fragments modify the total porosity evolution from the expected sintering curve (Fig. 3c). Yet, densification is evident in the total porosity reduction observed for the longer duration experiments, particularly in the fine-fragment systems which would experience faster sintering rates (e.g., Fig. 5a).

Previous studies have suggested that densification through sintering may have a limited impact on permeability until $\sim 0.25\tau_s$ (Wadsworth et al., 2017b), which is beyond the experiment duration for our samples. This is consistent with our observation that permeability is not substantially impacted by sintering in our experiments. We expect that longer durations at high temperature would cause further densification and result in more substantial permeability reduction. For hydrous systems, we may therefore expect that aggregates of fine fragments at $Pe \ll 1$ will rapidly expel their volatiles through diffusive outgassing and closely follow anhydrous porosity and permeability models (regime I, Fig. 4a). For aggregates of intermediate fragments (including our full fragment size range), connected porosity and permeability may reduce whilst dominated by vesiculation, and then subsequently increase again during diffusive outgassing, and finally, experience a second reduction during sintering (regimes II and III, Fig. 4a). For aggregates of coarse fragments at $Pe \gg 1$, connected porosity and permeability decrease first during vesiculation and then decrease further during sintering, whilst the impacts of diffusive outgassing are increasingly muted as the fragment size increases.

4.3. Analytical approximation of porosity in hydrous fragmental systems

To approximate the impact of sintering, vesiculation, and diffusive outgassing on the isolated and connected porosity of hydrous fragmental systems, we employ previously established models for densification through sintering (Wadsworth et al., 2019), closed system bubble growth (Coumans et al., 2020), and one-dimensional diffusion scaling (von Aulock et al., 2017). However, as sintering is the last process to complete for our experimental conditions (Fig. 4b), we first opt to disregard sintering and only estimate the volumetric impact of vesiculation and diffusive outgassing on the isolated pore space. Following Weaver et al. (2022), we consider individual spherical particles with initial volume $V_{I(0)} = \frac{4}{3}\pi r^3$, subject to the following steps; (1) the evolution of vesicularity $\phi(t)$ is estimated for a closed system using the bubble growth model from Coumans et al. (2020), as described in Section 4.1; (2) the rind thickness $d_l(t)$ is subtracted from the initial apparent fragment radius r to partition the spherical volume into a shrinking hydrous interior $V_{int(0)} = \frac{4}{3}\pi (r - d_l(t))^3$ and a thickening dehydrated rind; (3) the interior volume $V_{int(0)}$ is expanded by the vesicularity $\phi(t)$; (4) the evolving vesicular interior V_{int} and dense rind volumes are summed to provide the bulk skeletal fragment volume $V_I(t)$ throughout vesiculation and diffusive outgassing (Equation (4));

$$V_I(t) = -\frac{V_{int}}{(\phi(t) - 1)} + V_{I(0)} - V_{int}. \quad (4)$$

The bulk, open-system vesicularity for a fragment is then given by $\phi_i(t) = 1 - V_{I(0)}/V_I(t)$. For a monodisperse fragmental system which has not isolated any pore space through sintering, the development of any isolated porosity would be attributed (and so equal) to the vesicularity.

Given that the isolated and connected pore volumes are inversely proportional whilst $t < \tau_d$ (Fig. 5), we can approximate the connected porosity of a monodisperse fragmental system by first

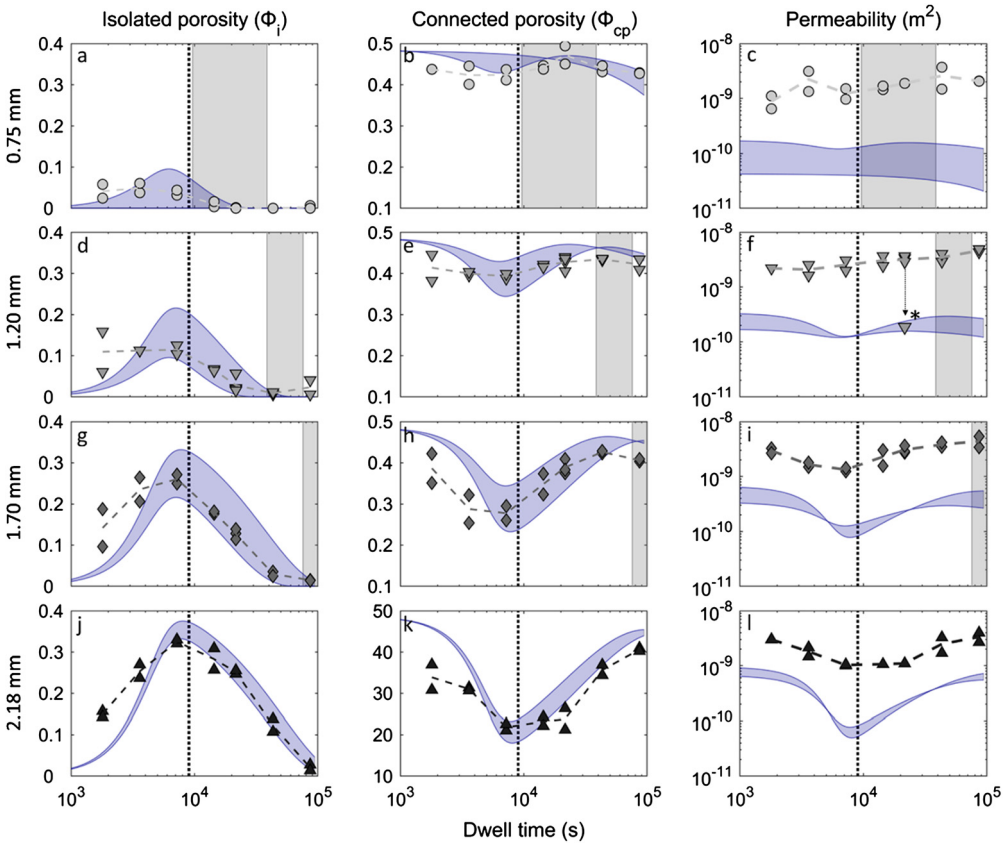

Fig. 6. The isolated sample porosities ϕ_i (column 1) and connected sample porosities ϕ_{cp} (column 2) are compared to a fragment size-dependent geometrical approximation for vesiculation, diffusive outgassing, and sintering (blue shading). The sample permeabilities (column 3), measured under unconfined conditions, are compared to modelled values using the modelled connected porosities and a permeability model (Wadsworth et al., 2016b). The vesiculation timescale τ_d is displayed as a vertical dotted black line, whilst the range in diffusive outgassing timescales is shown by the grey shaded vertical region. The one sample permeability remeasured with confining pressure is highlighted with an asterisk in panel f.

estimating the skeletal volume evolution of the system $V_{I*}(t)$, in which sintering does not isolate any pore space (Equation (5)),

$$V_{I*}(t) = \frac{-\rho_f V_T}{\phi_i - 1}, \tag{5}$$

where ρ_f is the fragment packing fraction and V_T is the total volume of the system. The evolving connected porosity $\phi_c(t)$ is then calculated using $\phi_c(t) = 1 - V_{I*}(t)/V_T$.

To incorporate the impact of sintering on the connected porosities, we first consider the resultant densification in isolation using the non-vesiculating sintering model of Wadsworth et al. (2016a). The rate of change in connected porosity is given by a numerical solution to

$$\frac{d\phi_{cp}}{dt} = -\frac{3\Gamma}{2\mu a_o}\left(\frac{\phi_{co}}{1-\phi_{co}}\right)^{1/3}\phi_{cp}^{2/3}\left(1-\phi_{cp}\right)^{1/3}, \tag{6}$$

where the viscosity μ is estimated using the water content of the dehydrated, outgassed rind (Hess and Dingwell, 1996), and the initial pore size a_o accounts for the relatively monodisperse particle size distribution of our experiments, following Wadsworth et al. (2017a). The pore volume evolution through sintering is then calculated by $V_s(t) = V_T\phi_{cp}(t)$.

To assess how concurrent sintering, vesiculation and diffusive outgassing impacts the connected porosity, we combine the results from Equation (5) and Equation (6), assuming, for simplicity, that the two equations (and the underlying processes) do not interfere with one another. With this caveat, we estimate the connected pore volume evolution of monodisperse, vesiculating, diffusively outgassing, and sintering fragmental systems $V_{C*}(t)$, where $V_{C*}(t) = V_T - V_{I*}(t) - (V_{S(0)} - V_S(t))$. The estimated connected porosity evolution $\phi_{c*}(t)$ is then calculated using $\phi_{c*}(t) = 1 - (V_T - V_{C*}(t))/V_T$.

By assuming that densification during sintering progresses independently from the physical impacts of vesiculation and diffusive outgassing, we do not account for complex interactions and feedback mechanisms, such as: fragment expansion increasing the melt contact area and thereby increasing the healing surface (e.g., Lamur et al., 2019) and fragment agglutination rate; sintering reducing the surface area of the aggregate (e.g., Wadsworth et al., 2021) and thus hindering the effectiveness of diffusive outgassing; and vesicular fragments being subject to intra-fragment interfacial forces acting between the vesicles and surrounding melt films (e.g., Mangan and Sisson, 2005), thereby disrupting the surface tension driven contraction of the particulate. Despite this simplification, we find that the model outlined here for a monodisperse system provides a close approximation to the evolution of the isolated and connected porosities of our samples (Fig. 6).

The impact of fragment size on the porosity distribution is captured to a reasonable extent, and we find that τ_d is a useful measure for determining the time required to fully densify fragments (see τ_d range in Fig. 6). Furthermore, when the approximation for the connected porosity is input into the porosity-permeability model of Wadsworth et al. (2016b), following the details in Section 3, we obtain an estimate for the permeability evolution in sintering, hydrous fragmental melts, which shares similar attitudes to our data (Fig. 6). As such, we suggest that our approach is appropriate when τ_b and τ_d are much shorter than τ_s, such that sintering can be considered to progress relatively unimpeded. The underestimation of modelled permeability of approximately one

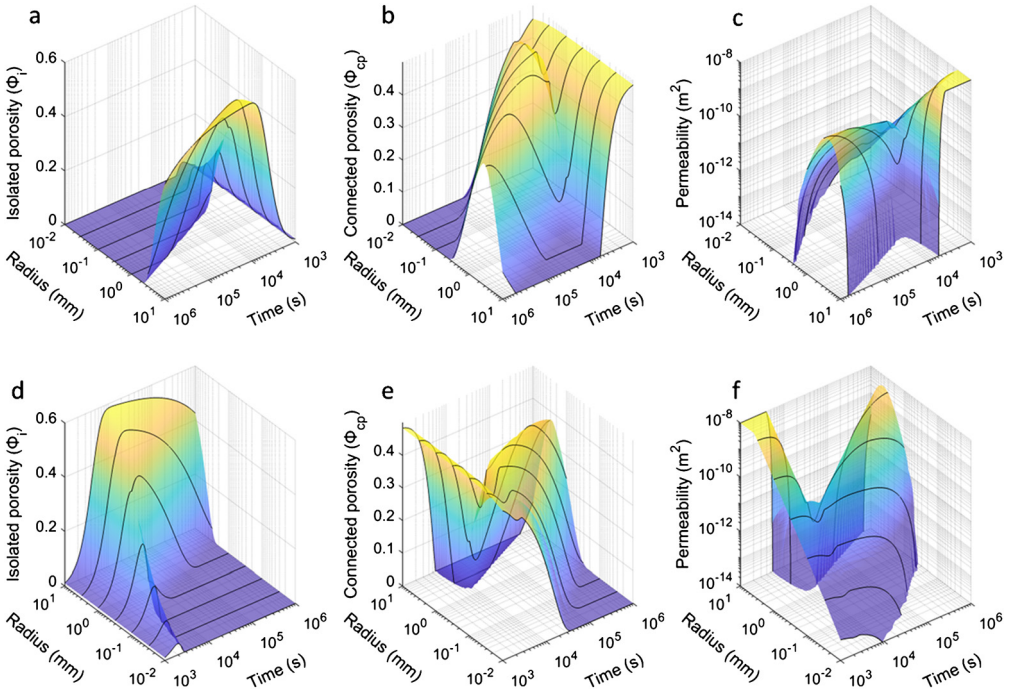

Fig. 7. Modelled (a) isolated porosity ϕ_i, (b) connected porosity ϕ_{cp}, and (c) permeability due to vesiculation, diffusive outgassing, and sintering of hydrous melt fragments in open-system conditions. (d-f) alternate view of the top row. Contours highlight fragment radius at every half log unit, the colours are defined by the vertical axis and are added to aid interpretation of the 3D geometry. Note that vesiculation causes a drop in connected porosity and permeability, which is reversed by diffusive outgassing. Densification via sintering overlays this transient behaviour and causes a progressive loss in connected porosity and permeability.

order of magnitude, as compared to our unconfined permeability measurements, can tentatively be attributed to the lack of confining pressure on the samples, noting the Wadsworth et al. (2016b) model was developed from measurements made with confinement. Our permeability measurements made with 1 MPa confining pressure for the 1.2 mm material (removed from the crucible) fall within the modelled range (Fig. 6f).

This modelling reinforces the importance of fragment size when considering the evolution of porosity and permeability in hydrous fragmental melts (see Fig. 7), which maintain an open system and a partial pressure differential with the surrounding gas. Extrapolating the relationship between fragment size and the minimum connected porosity, we suggest that, under certain conditions, the connected porosity may reach zero (Fig. 7b, e) and so, the system could momentarily seal due to the sole action of vesiculation (Fig. 7). This scenario occurs when the skeletal melt volume equals the total system volume ($V_{l*}(t) \approx V_T$), such that all inter-fragment pore space is lost, which marks the limit of the open systems studied here. This may be achieved by considerable vesiculation of monodisperse fragments (i.e., coarse and significantly oversaturated) or by less substantial vesiculation in densely packed fragmental systems, as might occur with high polydispersity. We thus anticipate that sealing by vesiculation may be applicable for a wider range of particle size distributions and occur much earlier than via sintering-induced densification, and we surmise that future efforts should explore a wider range of conditions (i.e., polydispersity, Peclet numbers, crystallinity, etc) to ascertain this.

4.4. Implications for natural fragmental melts

Understanding the evolution, distribution, and connectivity of porosity in fragmental melts, and the resulting permeability, is key for resolving the development of preserved pyroclastic systems through textural analysis (e.g., Colombier et al., 2017) and for constraining gas emissions as well as volcanic activity (e.g., Heap et al., 2019; Kolzenburg et al., 2019). Our analyses highlight that coarse oversaturated fragmental melts which experience a partial pressure differential with their surrounding gas may evolve in a complex manner compared with very fine particles that do not vesiculate (e.g., Wadsworth et al., 2021). Careful assessment of particle size distributions is required to determine the fragment size dependent porosity and permeability evolution during sintering of dehydrating systems; fine melt fragments may diffusively outgas without vesiculating and closely follow anhydrous porosity–permeability relationships, as shown in Wadsworth et al. (2021); coarser fragments attain higher and more long-lived vesicularities, which lead to substantial but transient losses in connected porosity and permeability of agglutinates.

For certain conditions (e.g., fragments are sufficiently hydrous, coarse, or densely packed) vesiculation can shut all intergranular void space, and the system may seal permeable pathways more rapidly than sintering alone, potentially inhibiting gas emissions and promoting gas accumulation and pressurisation. Sealing through vesiculation accounts for the textures present in fragmental infill (Fig. 1a), where vesicular melt parcels are separated by agglutinated dense rinds (cf. Cabrera et al., 2011; Castro et al., 2012; Giachetti et al., 2019; Heap et al., 2019; Saubin et al., 2016; Schipper et al., 2021). Where systems do not seal (e.g., in surficial or shallow environments, where deposits may not necessarily be compacted), the transience of vesicularity suggests that dense melt fragments should not necessarily be taken at face value as they may have vesiculated and subsequently densified through bubble resorption (see Fig. 2). Therefore, in volcanic conduits where localised fragmentation is prevalent (e.g., Schipper et al., 2021), diffusive outgassing from pyroclasts provides an effective means of dehydrating magma, which, following further sintering, may produce dense and dry melts (as suggested by Wadsworth et al., 2020a).

The new insights we have made into porosity and permeability evolution in complex sintering systems relevant to natural volcanic systems may be applied to shallow conduits (e.g., Schipper et al., 2021), tuffisite infill (e.g., Saubin et al., 2016), in-conduit sintering

during pyroclast transport (e.g., Giachetti et al., 2021), and ignimbrites (e.g., Lavallée et al., 2015), and the simple models we provide may prove useful for determining the longevity and efficiency of open gas venting networks.

4.5. Conclusions

Through the use of novel experiments, we highlight that the evolution of coarse hydrous fragmental melts is not captured by classical sintering models and instead, their porosity and permeability evolution is partly controlled by vesiculation and diffusive outgassing. The nucleation and growth of bubbles progressively expands melt fragments into the inter-fragment pore space, which loses connectivity and permeability. However, when fragments are in an open system, vesiculation acts in competition with diffusive outgassing, during which, volatile resorption densifies melt fragments' margins, increases the inter-fragment pore space, and enhances permeability. We highlight that the effectiveness of diffusive outgassing is determined by the surface area of pyroclasts, such that finer fragments attain lower vesicularities and lose vesicles faster than those of coarse fragments. Very fine pyroclasts may diffusively outgas all supersaturated volatiles prior to the onset of vesiculation, and therefore essentially follow non-vesiculating sintering models for dehydrated fragments. These processes induce complex porosity and permeability hysteresis. We show that this behaviour can be described using the timescales for the completion of sintering, vesiculation, and diffusive outgassing, and that the porosity-permeability development can be assessed through the integration of existing models for bubble growth, diffusion lengthscale, and surface tension driven densification. Our data and analyses may help to illuminate the textural history of glassy pyroclastic systems and constrain the porosity-permeability evolution of natural melt systems as well as their densification efficiency during shallow volcanic venting.

CRediT authorship contribution statement

J. Weaver: Writing – review & editing, Writing – original draft, Validation, Methodology, Investigation, Formal analysis. **A. Lamur:** Writing – review & editing, Writing – original draft, Methodology, Investigation, Formal analysis. **T.D. Lea:** Methodology, Investigation. **F.B. Wadsworth:** Writing – review & editing, Writing – original draft, Validation, Methodology, Investigation. **J.E. Kendrick:** Writing – review & editing, Writing – original draft, Visualization, Validation, Supervision, Methodology, Investigation, Conceptualization. **J. Schauroth:** Methodology, Investigation. **Y. Lavallée:** Writing – review & editing, Writing – original draft, Validation, Supervision, Resources, Project administration, Methodology, Investigation, Conceptualization.

Declaration of competing interest

The authors declare that they have no known competing financial interests or personal relationships that could have appeared to influence the work reported in this paper.

Data availability

Data will be made available on request.

Acknowledgements

This study has been conducted as part of a PhD funded by the Natural Environment Research Council (NERC) EAO Doctoral Training Partnership (NE/L002469/1) and the Landsvirkjun National Power Company of Iceland. Y. Lavallée kindly acknowledges financial support from a Consolidator Grant from the European Research Council (ERC) on *Magma outgassing during Eruptions and Geothermal Exploration* (MODERATE, no. 101001065). We also acknowledge financial support from two NERC grants (NE/T007796/1 and NE/X015440/1). This research project/publication was supported by LMUexcellent, funded by the Federal Ministry of Education and Research (BMBF) and the Free State of Bavaria under the Excellence Strategy of the Federal Government and the Länder.

Appendix A. Supplementary material

Supplementary material related to this article can be found online at https://doi.org/10.1016/j.epsl.2023.118410.

References

Bagdassarov, N.S., Dingwell, D.B., Wilding, M.C., 1996. Rhyolite magma degassing: an experimental study of melt vesiculation. Bull. Volcanol. 57, 587–601.
Blower, J.D., Mader, H.M., Wilson, S.D.R., 2001. Coupling of viscous and diffusive controls on bubble growth during explosive volcanic eruptions. Earth Planet. Sci. Lett. 193, 47–56.
Branney, M.J., Kokelaar, P., Kokelaar, B.P., 2002. Pyroclastic density currents and the sedimentation of ignimbrites.
Cabrera, A., Weinberg, R.F., Wright, H.M.N., Zlotnik, S., Cas, R.A.F., 2011. Melt fracturing and healing: a mechanism for degassing and origin of silicic obsidian. Geology 39, 67–70.
Castro, J.M., Cordonnier, B., Tuffen, H., Tobin, M.J., Puskar, L., Martin, M.C., Bechtel, H.A., 2012. The role of melt-fracture degassing in defusing explosive rhyolite eruptions at volcán Chaitén. Earth Planet. Sci. Lett. 333, 63–69.
Colombier, M., Wadsworth, F.B., Gurioli, L., Scheu, B., Kueppers, U., Di Muro, A., Dingwell, D.B., 2017. The evolution of pore connectivity in volcanic rocks. Earth Planet. Sci. Lett. 462, 99–109.
Coumans, J.P., Llewellin, E.W., Wadsworth, F.B., Humphreys, M.C.S., Mathias, S.A., Yelverton, B.M., Gardner, J.E., 2020. An experimentally validated numerical model for bubble growth in magma. J. Volcanol. Geotherm. Res. 402, 107002.
Gardner, J.E., Wadsworth, F.B., Llewellin, E.W., Watkins, J.M., Coumans, J.P., 2018. Experimental sintering of ash at conduit conditions and implications for the longevity of tuffisites. Bull. Volcanol. 80, 23.
Giachetti, T., Druitt, T.H., Burgisser, A., Arbaret, L., Galven, C., 2010. Bubble nucleation, growth and coalescence during the 1997 Vulcanian explosions of Soufrière Hills Volcano, Montserrat. J. Volcanol. Geotherm. Res. 193, 215–231.
Giachetti, T., Gonnermann, H.M., 2013. Water in volcanic pyroclast: rehydration or incomplete degassing? Earth Planet. Sci. Lett. 369, 317–332.
Giachetti, T., Gonnermann, H.M., Gardner, J.E., Burgisser, A., Hajimirza, S., Earley, T.C., Truong, N., Toledo, P., 2019. Bubble coalescence and percolation threshold in expanding rhyolitic magma. Geochem. Geophys. Geosyst. 20, 1054–1074.
Giachetti, T., Trafton, K.R., Wiejaczka, J., Gardner, J.E., Watkins, J.M., Shea, T., Wright, H.M.N., 2021. The products of primary magma fragmentation finally revealed by pumice agglomerates. Geology 49, 1307–1311.
Heap, M.J., Tuffen, H., Wadsworth, F.B., Reuschlé, T., Castro, J.M., Schipper, C.I., 2019. The permeability evolution of tuffisites and implications for outgassing through dense rhyolitic magma. J. Geophys. Res., Solid Earth 124, 8281–8299.
Hess, K.U., Dingwell, D.B., 1996. Viscosities of hydrous leucogranitic melts: a non-Arrhenian model. Am. Mineral. J. Earth Planet. Mater. 81, 1297–1300.
Kolzenburg, S., Russell, J.K., 2014. Welding of pyroclastic conduit infill: a mechanism for cyclical explosive eruptions. J. Geophys. Res., Solid Earth 119, 5305–5323.
Kolzenburg, S., Ryan, A.G., Russell, J.K., 2019. Permeability evolution during non-isothermal compaction in volcanic conduits and tuffisite veins: implications for pressure monitoring of volcanic edifices. Earth Planet. Sci. Lett. 527, 115783.
Lamur, A., Kendrick, J.E., Wadsworth, F.B., Lavallée, Y., 2019. Fracture healing and strength recovery in magmatic liquids. Geology 47, 195–198.
Lamur, A., Lavallée, Y., Iddon, F.E., Hornby, A.J., Kendrick, J.E., von Aulock, F.W., Wadsworth, F.B., 2018. Disclosing the temperature of columnar jointing in lavas. Nat. Commun. 9, 1–7.
Lavallée, Y., Wadsworth, F.B., Vasseur, J., Russell, J.K., Andrews, G.D.M., 2015. Eruption and emplacement timescales of ignimbrite super-eruptions from thermokinetics of glass shards. Front. Earth Sci. 3, 2.
Mangan, M., Sisson, T., 2005. Evolution of melt-vapor surface tension in silicic volcanic systems: experiments with hydrous melts. J. Geophys. Res., Solid Earth 110.
McIntosh, I.M., Llewellin, E.W., Humphreys, M.C.S., Nichols, A.R.L., Burgisser, A., Schipper, C.I., Larsen, J.F., 2014. Distribution of dissolved water in magmatic glass records growth and resorption of bubbles. Earth Planet. Sci. Lett. 401, 1–11.
Navon, O., Lyakhovsky, V., 1998. Vesiculation processes in silicic magmas. Geol. Soc. (Lond.) Spec. Publ. 145, 27–50.

Ohsawa, S., Yusa, Y., Oue, K., Amita, K., 2000. Entrainment of atmospheric air into the volcanic system during the 1995 phreatic eruption of Kuju Volcano, Japan. J. Volcanol. Geotherm. Res. 96, 33–43.
Otsuki, S., Nakamura, M., Okumura, S., Sasaki, O., 2015. Interfacial tension-driven relaxation of magma foam: an experimental study. J. Geophys. Res., Solid Earth 120, 7403–7424.
Parikh, N.M., 1958. Effect of atmosphere on surface tension of glass. J. Am. Ceram. Soc. 41, 18–22.
Pitzer, K.S., Sterner, S.M., 1994. Equations of state valid continuously from zero to extreme pressures for H2O and CO2. J. Chem. Phys. 101, 3111–3116.
Quane, S.L., Russell, J.K., 2005. Welding: insights from high-temperature analogue experiments. J. Volcanol. Geotherm. Res. 142, 67–87.
Rust, A.C., Cashman, K.V., Wallace, P.J., 2004. Magma degassing buffered by vapor flow through brecciated conduit margins. Geology 32, 349–352.
Ryan, A.G., Russell, J.K., Hess, K.-U., Phillion, A.B., Dingwell, D.B., 2015a. Vesiculation in rhyolite at low H2O contents: a thermodynamic model. Geochem. Geophys. Geosyst. 16, 4292–4310.
Ryan, A.G., Russell, J.K., Nichols, A.R.L., Hess, K.-U., Porritt, L.A., 2015b. Experiments and models on H2O retrograde solubility in volcanic systems. Am. Mineral. 100, 774–786.
Saubin, E., Tuffen, H., Gurioli, L., Owen, J., Castro, J.M., Berlo, K., McGowan, E.M., Schipper, C.I., Wehbe, K., 2016. Conduit dynamics in transitional rhyolitic activity recorded by tuffisite vein textures from the 2008–2009 Chaitén Eruption. Front. Earth Sci. 4, 59.
Schipper, C.I., Castro, J.M., Kennedy, B.M., Tuffen, H., Whattam, J., Wadsworth, F.B., Paisley, R., Fitzgerald, R.H., Rhodes, E., Schaefer, L.N., et al., 2021. Silicic conduits as supersized tuffisites: clastogenic influences on shifting eruption styles at Cordón Caulle volcano (Chile). Bull. Volcanol. 83, 1–22.
Seropian, G., Kennedy, B.M., Kendrick, J.E., Lavallée, Y., Nichols, A.R.L., Von Aulock, F.W., Dingwell, D.B., Hess, K.-U., Lamur, A., Schauroth, J., Vasseur, J., Wadsworth, F.B., 2022. Vesiculation of rhyolitic melts under oscillatory pressure. Front. Earth Sci. 219.
Sparks, R.S.J., 1978. The dynamics of bubble formation and growth in magmas: a review and analysis. J. Volcanol. Geotherm. Res. 3, 1–37.
Tuffen, H., Castro, J.M., 2009. The emplacement of an obsidian dyke through thin ice: Hrafntinnuhryggur, Krafla Iceland. J. Volcanol. Geotherm. Res. 185, 352–366.
Tuffen, H., Dingwell, D., 2005. Fault textures in volcanic conduits: evidence for seismic trigger mechanisms during silicic eruptions. Bull. Volcanol. 67, 370–387. https://doi.org/10.1007/s00445-004-0383-5.
Unwin, H.E., Tuffen, H., Phillips, E., Wadsworth, F.B., James, M.R., 2021. Pressure-driven opening and filling of a volcanic hydrofracture recorded by tuffisite at Húsafell, Iceland: a potential seismic source. Front. Earth Sci. 9, 347.
Vasseur, J., Wadsworth, F.B., Lavallée, Y., Hess, K.-U., Dingwell, D.B., 2013. Volcanic sintering: timescales of viscous densification and strength recovery. Geophys. Res. Lett. 40, 5658–5664.
von Aulock, F.W., Kennedy, B.M., Maksimenko, A., Wadsworth, F.B., Lavallée, Y., 2017. Outgassing from open and closed magma foams. Front. Earth Sci. 5, 46.
Wadsworth, F.B., Llewellin, E.W., Vasseur, J., Gardner, J.E., Tuffen, H., 2020a. Explosive-effusive volcanic eruption transitions caused by sintering. Sci. Adv. 6, eaba7940.
Wadsworth, F.B., Vasseur, J., Llewellin, E.W., Brown, R.J., Tuffen, H., Gardner, J.E., Kendrick, J.E., Lavallée, Y., Dobson, K.J., Heap, M.J., et al., 2021. A model for permeability evolution during volcanic welding. J. Volcanol. Geotherm. Res. 409, 107118.
Wadsworth, F.B., Vasseur, J., Llewellin, E.W., Dingwell, D.B., 2017a. Sintering of polydisperse viscous droplets. Phys. Rev. E 95, 33114.
Wadsworth, F.B., Vasseur, J., Llewellin, E.W., Dobson, K.J., Colombier, M., Von Aulock, F.W., Fife, J.L., Wiesmaier, S., Hess, K.-U., Scheu, B., et al., 2017b. Topological inversions in coalescing granular media control fluid-flow regimes. Phys. Rev. E 96, 33113.
Wadsworth, F.B., Vasseur, J., Llewellin, E.W., Schauroth, J., Dobson, K.J., Scheu, B., Dingwell, D.B., 2016a. Sintering of viscous droplets under surface tension. Proc. R. Soc. A, Math. Phys. Eng. Sci. 472, 20150780.
Wadsworth, F.B., Vasseur, J., Schauroth, J., Llewellin, E.W., Dobson, K.J., Havard, T., Scheu, B., von Aulock, F.W., Gardner, J.E., Dingwell, D.B., et al., 2019. A general model for welding of ash particles in volcanic systems validated using in situ X-ray tomography. Earth Planet. Sci. Lett. 525, 115726.
Wadsworth, F.B., Vasseur, J., Scheu, B., Kendrick, J.E., Lavallée, Y., Dingwell, D.B., 2016b. Universal scaling of fluid permeability during volcanic welding and sediment diagenesis. Geology 44, 219–222.
Wadsworth, F.B., Vossen, C.E.J., Schmid, D., Colombier, M., Heap, M.J., Scheu, B., Dingwell, D.B., 2020b. Determination of permeability using a classic Darcy water column. Am. J. Phys. 88, 20–24.
Weaver, J., Lavallée, Y., Ashraf, M., Kendrick, J.E., Lamur, A., Schauroth, J., Wadsworth, F.B., 2022. Vesiculation and densification of pyroclasts: a clast-size dependent competition between bubble growth and diffusive outgassing. J. Volcanol. Geotherm. Res. 107550.
Yoshimura, S., Nakamura, M., 2008. Diffusive dehydration and bubble resorption during open-system degassing of rhyolitic melts. J. Volcanol. Geotherm. Res. 178, 72–80.
Zhang, Y., Ni, H., 2010. Diffusion of H, C, and O components in silicate melts. Rev. Mineral. Geochem. 72, 171–225.